Chemistry–A European Journal

Research Article
doi.org/10.1002/chem.202400565

Chemistry Europe
European Chemical Societies Publishing

www.chemeurj.org

Determining Structures of Layer-by-Layer Spin-Coated Zinc Dicarboxylate-Based Metal-Organic Thin Films

Jan C. Fischer,[a] Robbin Steentjes,[b] Dong-Hui Chen,*[c] Bryce S. Richards,[a, d] Egbert Zojer,*[b] Christof Wöll,[c] and Ian A. Howard*[a, d]

Thin films of crystalline solids with substantial free volume built from organic chromophores and metal secondary building units (SBUs) are promising for engineering new optoelectronic properties through control of interchromophore coupling. Zn-based SBUs are especially relevant in this case because they avoid quenching the chromophore's luminescence. We find that layer-by-layer spin-coating using Zn acetate dihydrate and benzene-1,4-dicarboxylic acid (H_2BDC) and biphenyl-4,4′-dicarboxylic acid (H_2BPDC) linkers readily produces crystalline thin films. However, analysis of the grazing-incidence wide-angle X-ray scattering (GIWAXS) data reveals the structures of these films vary significantly with the linker, and with the metal-to-linker molar ratio used for fabrication. Under equimolar conditions, H_2BPDC creates a type of structure like that proposed for SURMOF-2, whereas H_2BDC generates a different metal-hydroxide-organic framework. Large excess of Zn^{2+} ions causes the growth of layered zinc hydroxides, irrespective of the linker used. Density functional theory (DFT) calculations provide structural models with minimum total energy that are consistent with the experimentally observed diffractograms. In the broader sense, this work illustrates the importance in this field of careful structure determination, *e.g.*, by utilizing GIWAXS and DFT simulations to determine the structure of the obtained crystalline metal-organic thin films, such that properties can be rationally engineered and explained.

Introduction

Metal-organic frameworks (MOFs) are an interesting class of optoelectronic materials. Their large lattice spacing and substantial free volumes are able to create unique interactions among metal centers, linkers, and guest molecules. MOFs have a variety of optoelectronic applications, ranging from luminescent sensing,[1,2] to upconversion and nonlinear optics,[3,4] and light-emitting devices.[5,6] There have also been recent advances in photo-responsive MOFs with semiconducting properties.[7,8] To integrate MOFs into devices, it is often desirable to grow or deposit them as oriented thin films on substrates. Potential applications of such thin films can comprise chemiresistive sensors,[9,10] photodetectors,[11] organic light-emitting diodes,[12] or solar cells.[13,14] There is a variety of synthesis routes targeted at generating oriented thin films, which have been presented in numerous reviews.[9,15] These include, for example, a solution-based heteroepitaxial growth on oriented substrates,[16] a vapor-assisted conversion within a sealed heated vessel,[17] or a two-step vapor-phase deposition utilizing a template layer.[18] However, one of the most commonly employed techniques is a layer-by-layer approach wherein a substrate is alternately exposed to solutions containing the metal salt and the organic linker precursors.[19] This alternating exposure of the substrate to different growth solutions can be achieved by using a pump system to cyclically exchange the solution in a growth vessel,[20,21] by moving and dipping the substrate into various solutions,[22] by alternately spraying solutions onto a substrate,[23,24] or by alternately spin-casting the two solutions onto a substrate.[25]

Characterizing the resulting structure of MOF thin films is not trivial, due to the very limited amount of crystalline material, and the limited number of reflections caught in one-dimensional out-of-plane and in-plane X-ray diffraction (XRD) measurements. Surface-sensitive techniques such as grazing-incidence XRD and grazing-incidence wide-angle X-ray scattering (GIWAXS), can mitigate these problems and have been proven to be an excellent tool for structure determination of MOF thin films often using synchrotron radiation,[18,26–29] and also laboratory-scale X-ray sources.[17,30] In a previous work, we

[a] J. C. Fischer, Prof. Dr. B. S. Richards, Dr. I. A. Howard
Institute of Microstructure Technology,
Karlsruhe Institute of Technology,
Hermann-von-Helmholtz-Platz 1,
76344 Eggenstein-Leopoldshafen, Germany
E-mail: iahoward@gmail.com

[b] R. Steentjes, Prof. Dr. E. Zojer
Institute for Solid-State Physics, NAWI Graz,
Graz University of Technology,
Petersgasse 16/II, 8010 Graz, Austria
E-mail: egbert.zojer@tugraz.at

[c] Dr. D.-H. Chen, Prof. Dr. C. Wöll
Institute of Functional Interfaces,
Karlsruhe Institute of Technology,
Hermann-von-Helmholtz-Platz 1,
76344 Eggenstein-Leopoldshafen, Germany
E-mail: donghui.chen@kit.edu

[d] Prof. Dr. B. S. Richards, Dr. I. A. Howard
Light Technology Institute,
Karlsruhe Institute of Technology,
Engesserstrasse 13, 76131 Karlsruhe, Germany

Supporting information for this article is available on the WWW under https://doi.org/10.1002/chem.202400565

utilized the GIWAXS method to test structural hypotheses against experimental data, in that case, focusing on UiO-66 thin films with Zr-containing secondary building units (SBUs) deposited by vapor-assisted conversion.[31] Here, we are interested in Zn-based structures of stacked layers that should be similar to those established in the significant work on Cu^{2+} based SBUs. These structures allow for the interaction of neighboring chromophores that influences their photo-responsive properties.[32,33] An example of a sought topology is the sheet-like structure suggested for surface-anchored MOF-2 (SURMOF-2), wherein four dicarboxylic linkers are assumed to surround a paddlewheel SBU in a square-planar configuration.[23,34,35] However, the Cu^{2+} ions often used in such systems are not attractive for light-emitting chromophores. The Cu^{2+} open shell configuration leads to rapid non-radiative deactivation of excited states via ligand-to-metal charge transfer, effectively preventing light emission.[36] This is not expected to happen for Zn^{2+} ions, because of their filled 3d atomic orbital.[36,37] While Cu-based systems may be better behaved in terms of consistently forming SURMOF-2, we find that this is not the case for Zn but a variety of different crystalline topologies can be formed in the layer-by-layer synthesis. Thus, special care must be taken in establishing the structure of the crystalline thin films formed when attempting to grow Zn-based SURMOF-2 type structures.

In this respect, we note that MOFs are not the only material system that can be created from dicarboxylic linkers and metal salts. Another structural motif that can be formed with the same precursors is given by layered metal hydroxides (LMHs), which are an interesting material class in their own right. For example, LMHs have long been known for their ability to intercalate and exchange (organic) anions.[38,39] In LMHs, many dense metal-containing layers are stacked over each other, each mainly consisting of octahedral sites with some tetrahedral sites at which acidic small molecules can be attached. Basic layered zinc hydroxide (LZH), for example, is often synthesized with intercalating acetic acid guest molecules.[40–42] Such guest molecules can be exchanged for other (*e.g.* longer) anions post-synthesis.[43,44] In their powder form, LMHs have been used as slow-release systems, for example for delivering drugs or pesticides.[45–47] Moreover, LZH has been explored as a matrix for holding organic luminescent sensitizers.[48–50] Beyond applications as host systems, LZH thin films can serve as precursor layers that transform into highly oriented ZnO crystals by heat treatment.[51–57] They also found application in organic solar cells as template layers and sensitizers.[53,54,58] There are numerous synthesis routes for generating LMH powders that are summarized in review articles.[38,39] However, there are fewer reports of the direct fabrication of LMH thin films. Some routes have been investigated that involve the precipitation onto substrates under solvothermal conditions, both with and without the usage of a liquid-liquid interface as a site for heterogeneous nucleation.[38,40,59,60] Electrodeposition is another method to grow LZH thin films on indium tin oxide substrates, even exhibiting some preferred orientation.[52–54,57] Finally, spin-casting of sol-gels has been presented as a possible route to LZH thin films.[61]

In this work, we investigate thin films made by layer-by-layer spin-casting, an easily accessible technique often used to target the SURMOF-2 structure. It has been shown that the precursor concentration in the growth solutions used for layer-by-layer MOF fabrication can have a significant impact on the resulting morphology.[62] In the literature of layer-by-layer MOF preparation, the concentration of the metal precursor solution is often much higher than that of the linker solution. Commonly, metal ion-to-linker molar ratios range from 10 : 1 to 50 : 1.[20,23–25,63–67] The stoichiometry of the targeted MOF structure does not reflect this ratio (for example in SURMOF-2 the stoichiometry is assumed to be 1 : 1 Zn^{2+} to linker). On this basis, we use a combination of dicarboxylic acid linkers and Zn precursor and test the resulting structures - *via* GIWAXS supported by density functional theory (DFT) calculations – for different Zn^{2+}-to-linker molar ratios ranging from a significant excess of the metal ions to equimolar conditions. Depending on the ratio, we find that significantly different structures can be obtained from layer-by-layer spin-casting, often strongly deviating from the initially expected SURMOF-2 type structure. We run these experiments with a variety of different linkers, but focus on benzene-1,4-dicarboxylic acid (H_2BDC) and biphenyl-4,4′-dicarboxylic acid (H_2BPDC). Zinc acetate dihydrate is used as the metal precursor. For ease of readability, in the following, we use the terminology Zn-BDC and Zn-BPDC for structures that were made from these precursors, respectively. GIWAXS observations reveal the substantial topological variations of the crystalline thin film structures created in our experiments with structural models derived from *ab initio* DFT calculations that fully explain the *a priori* unexpected diffraction patterns. From this detailed work, we conclude that an LZH structure tends to be formed in general (for all of the 4 linkers tested of widely varying length) when Zn^{2+} is in high excess with respect to the linker in the precursor solutions. At equimolar conditions, other structures are formed. The DFT-based interpretation of the GIWAXS data indicates that the H_2BDC linker then results in a dense, non-porous metal-hydroxide-organic framework (MHOF). For the H_2BPDC linker under equimolar conditions, a diffraction pattern strongly resembling its Cu-analog with peak positions consistent with those reported for SURMOF-2 in the literature is found. Testing intermediate excess levels of Zn^{2+} over BDC^{2-}, reveals the formation of mixed films of both the equimolar and LZH structures, until the LZH structure completely dominates (from metal ion-to-linker ratios of 50 : 1). The structural differences of the grown layers are confirmed by infrared-reflectance absorption spectroscopy (IRRAS), and visible photoluminescence (PL) data. For the future development of Zn-based crystalline metal-organic thin films these results show that a wide collection of structures can be created via simple spin-coating techniques. The work clearly demonstrates the variety of topologies at which organic chromophores can be assembled via the layer-by-layer spin-coating with Zn^{2+} metal centers, ranging from the intercalated chromophores between the dense ZnOH sheets of LZHs to creating stacked layers of the chromophores surrounding Zn SBUs. On the other hand, the work is cautionary in that efforts must be taken to determine

the structure in each case, as it can vary widely with the precise linker and synthesis conditions employed.

Results and Discussion

Overview of Structures Obtained

We based our experiments on common layer-by-layer spin-coating recipes used in the literature to fabricate MOF thin films.[25,32,68,69] The basic steps of this procedure are to alternately spin-cast metal and linker precursor solutions onto a substrate with intermediate ethanol rinsing steps. For our syntheses, we adopted the spin-coating protocol from Haldar *et al.*,[32] wherein the solution droplets are applied before substrate spinning, and spin time and speed are fixed to 10 s and 2000 rpm, respectively. Following this procedure, we grew thin films based on the two commonly used H_2BDC and H_2BPDC linkers, and Zn acetate dihydrate. We analyzed the obtained thin films with GIWAXS utilizing the approach presented previously[31] and employing a laboratory-scale Bruker D8 Advance with parallel beam optics and an area detector. Thereby, 2D scattering patterns are taken with the detector at different positions on a goniometer. These patterns are then projected onto a virtual, vertical image plane in order to analyze the diffractograms with standard open-source packages, such as GIXSGUI,[70] developed for use at synchrotron beamlines.

Figure 1 presents an overview of the 2D GIWAXS patterns observed from the BDC^{2-} linker with Cu-based SBUs (serving as the experimental reference of the 'desired' SURMOF-2 structure in Figure 1a, with an equimolar ratio of linker and Zn^{2+} precursor (Figure 1b), and with a high excess of the Zn^{2+} precursor (Figure 1c). In the right column of Figure 1 are analogous data for the H_2BPDC linker again showing the Cu-based reference, and the results for equimolar and excess Zn^{2+} precursor. The 2D GIWAXS diffractograms are plotted in reciprocal space coordinates q_z (out-of-plane component) and q_r (in-plane component for 2D powder materials). Considering the Cu reference structures, the peak positions in the GIWAXS patterns of Cu-BDC and Cu-BPDC shown in Figure 1a,d are consistent with reported diffraction data in the literature attributed to SURMOF-2. From these, experimental unit cell parameters ranging from 10.61 Å to 11.19 Å for H_2BDC and from 15.28 Å to 15.49 Å for H_2BPDC have been determined.[16,23,34] The inter-sheet spacing suggested in these experiments,[16,23,34] is almost invariant to a change of linkers, with 5.80 to 5.90 Å according to literature. If the stacked sheets are preferentially oriented lying flat on the substrate, then the inter-sheet scattering would be expected in the q_z axis and the scattering from the square in-sheet lattice in the q_r axis. However, for the spin-coating layer-by-layer fabrication approach, the preferential orientation is such that the suggested sheets stand perpendicular to the substrate plane. In this case, one expects to see a strong peak from the square unit cell in the q_z direction, a weaker peak from the square unit cell in the q_r direction due to random crystallite rotations about the substrate normal, and also a peak corresponding to the inter-sheet separation in the q_r direction. The axis crossings for the vertical orientation first order scattering peaks, according to the unit cell values from Friedländer *et al.* (10.71 Å, 15.28 Å and 5.80 Å),[34] are indicated by red bars in all panels of Figure 1. The observed peak positions in Figures 1a,d line up with the red bars, confirming that we have synthesized structures matching the literature of SURMOF-2, as expected.

These Cu-based thin films were made using a Cu^{2+}-to-linker ratio of 1:1 (at 0.1 mM absolute concentration of the precursor solutions). When employing the same synthesis protocol for Zn-BDC and Zn-BPDC, the 2D diffractograms shown in Figures 1b,e were obtained. The diffractogram for the H_2BPDC sample in Figure 1e agrees well its Cu-based analog, suggesting the same SURMOF-2 type structure and texture also for Zn-BPDC. This is, however, not the case for the H_2BDC linker (see panel b): in the q_z direction we observe a small but clear deviation of the peak position compared to the Cu-BDC reference amounting to ~0.04 $Å^{-1}$, which translates to a significant difference of ~0.6 Å in scattering plane distances. Moreover, the scattering pattern in q_r direction is visibly altered and additionally shows a faint maximum at ~1.00 $Å^{-1}$. We will examine this Zn-BDC (1:1) structure in more detail in a later section, where we propose a model resulting from *ab initio* calculations, and which we refer to as metal-hydroxide-organic framework (MHOF), a terminology proposed by Yuan *et al.*, because of the strong similarity to their Ni-based systems.[71] Now, however, we return to the overview to consider the scattering patterns obtained at high Zn^{2+} excess.

The results for 50:1 Zn^{2+}-to-linker ratios (with a Zn precursor absolute concentration of 1 mM), are shown in Figures 1c and 1f. In this case, neither of the diffraction patterns of Zn-BDC or Zn-BPDC are even reminiscent of the diffractogram of SURMOF-2 in any orientation. The pronounced maxima along the q_z axis in Figures 1c and 1f indicate strong ordering in the out-of-plane direction - *i.e.*, there is a long-range periodic arrangement normal to the substrate. Conversely, there are no visible diffraction maxima in the in-plane direction. The values for the out-of-plane layer separations, with ~14.3 Å in the case of Zn-BDC and ~18.8 Å for Zn-BPDC, resulting from the diffractograms are significantly larger than expected for SURMOF-2. From these qualitative observations, we can already conclude that the structures corresponding to the diffractograms in Figures 1c,f are not of the SURMOF-2 type. In the following section, we will investigate this more thoroughly, and provide strong evidence that these structures are, in fact, LZH thin films.

To conclude this section, we note that, to conveniently compare the position of diffraction maxima from the GIWAXS data with powder XRD (PXRD) data in the literature, we generated pseudo-powder XRD (pPXRD) patterns by performing radial integrations of the 2D GIWAXS data. The resulting plots are given in Figure S1, which for the cases of Cu-BDC and Cu-BPDC and Zn-BPDC (1:1) show a good agreement with PXRD patterns reported for the SURMOF-2 structure,[16,23,34] while there is no agreement for the other samples.

Finally, it should be mentioned that we are aware that there has been an ongoing discussion about the true nature of the

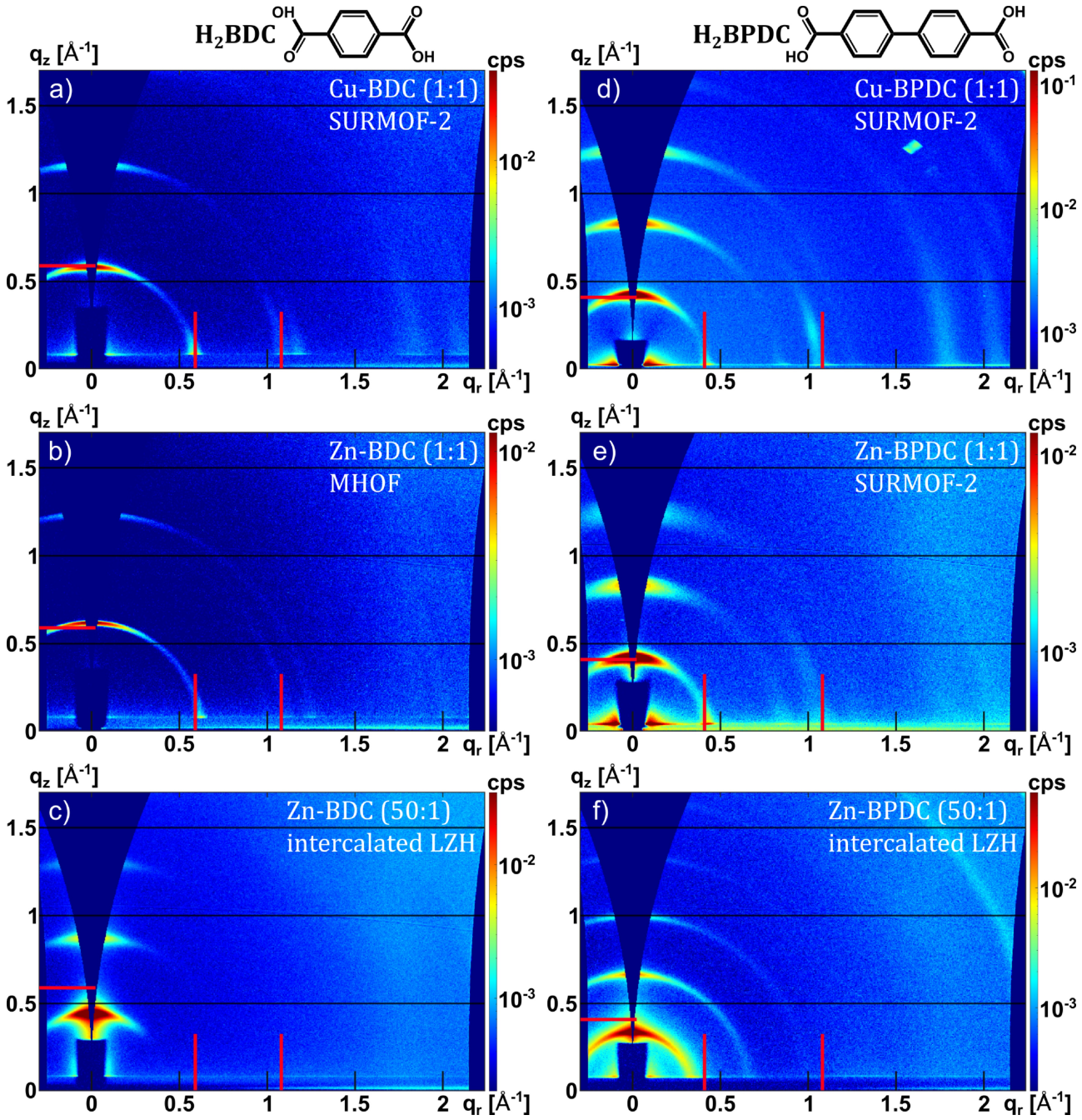

Figure 1. GIWAXS patterns of layer-by-layer spin-coated thin films illustrating the different structures obtained by varying the Zn^{2+}-to-linker ratios. a–c) show H_2BDC structures and d–f) H_2BPDC structures with the metal ion-to-linker ratios indicated. For comparison, the Cu-based analogs in which metal centers and linkers form a SURMOF-2 type structure are shown at the top (a, d). Red bars indicate important in- and out-of-plane scattering from a vertically oriented SURMOF-2 type structure and black horizontal lines serve as further visual aid to compare the patterns.

SURMOF-2 structure within the community. However, a detailed investigation of this topic is beyond the scope of this work and we restrict the discussion to diffractograms being equivalent (or not) to the SURMOF-2 data available in literature, without eluding to the details of the underlying atomistic structure. Instead, we focus on clarifying the arrangement of atoms and molecules for the different Zn-based thin films obtained by varying the precursor concentrations. This in itself is far from trivial. Detailed refinements of the precise atomic arrangements in the SURMOF-2 system are ongoing and will be discussed elsewhere.

Dicarboxylate-Intercalated Layered Zinc Hydroxide (LZH)

Taking a closer look at the diffractograms of the Zn-BDC and Zn-BPDC structures in Figures 1c, f, in addition to the main features that appear in the q_z direction, faint ring-like features

can be seen at higher q-values (meaning shorter scattering plane distances). In Figure 1c, they are hardly resolved, but in the diffractogram of the much less surface-oriented Zn-BPDC sample in Figure 1f one sees a very clear ring just above 2 $Å^{-1}$. To characterize this high-q scattering and to gain a more complete understanding of the structure of that film, we show the multi frame GIWAXS image capturing the 2D diffractogram up to a scattering vector of approximately 4 $Å^{-1}$ in Figure 2a. Interestingly, this image shows a very distinct set of diffraction peaks originating from three different crystal spacings: The main peak (and ring) at $q \approx 0.33$ $Å^{-1}$ and its higher orders at ~0.66 and ~0.99 $Å^{-1}$ highlighted in pink and labeled as (010), (020), and (030), the ring at $q \approx 2.30$ $Å^{-1}$ highlighted in orange and labeled as (002) and the ring at ~3.99 $Å^{-1}$ highlighted in green and labeled as (400). This type of diffraction fingerprint perfectly matches the LZH structure, which may be even more apparent by generating the pPXRD pattern from the GIWAXS data (Figure 2b).[40,42,44,72–74] The reduced subset of visible

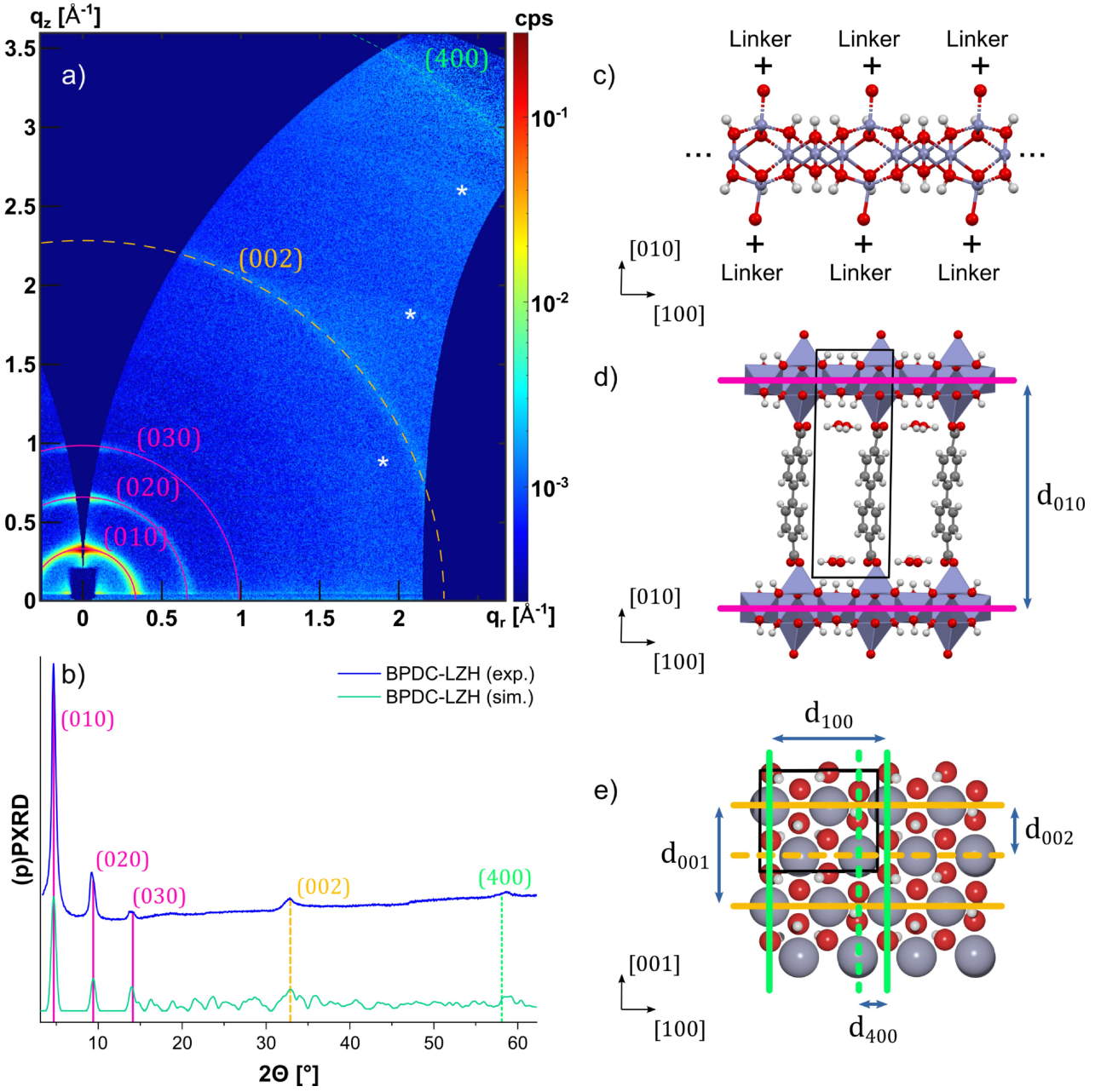

Figure 2. $BPDC^{2-}$-intercalated layered zinc hydroxide (LZH). a) GIWAXS of BPDC-LZH thin film. b) pPXRD generated by radially integrating the GIWAXS data and simulated PXRD based on the DFT-optimized BPDC-LZH structural model. c–e) Different views of the optimized model for BPDC-LZH with indication of important scattering planes. The Debye rings in the GIWAXS diffractogram and peaks in the pPXRD labeled as (010) and higher orders thereof, in pink, correspond to interlayer scattering, as illustrated in (d). The rings and peaks labeled as (002), in orange, and (400), in green, correspond to Zn–Zn distances within the ZnOH sheets, sketched in e. The step-like variation in background noise labeled by white asterisks in the diffractogram are systemic due to the stitching of images from different detector positions. The large dark-blue areas correspond to regions in the q_z-q_r plane unobservable in the GIWAXS measurement.

diffraction peaks contrasts the multitude of PXRD peaks simulated for a perfectly crystalline structure, also shown in the figure for comparison. It is an indication of turbostratic disorder which is commonly observed in LZHs and results from neighboring ZnOH sheets being rotated and/or translated with respect to each other while their common layer spacing is preserved.[75,76]

Starting from models in the literature (see Section S1), we created a DFT-optimized structure for the BPDC-LZH structure, shown in Figures 2c to 2e. Dense zinc hydroxide layers are separated by dicarboxylate linkers. We can assign the lower angle diffraction maxima (lower q values) to the basal layer spacing between zinc hydroxide sheets which is directly associated with the length of the dicarboxylate used for fabrication (more on this specific aspect later). In the current case of an H_2BPDC-based LZH, this basal spacing is fully consistent with our density functional theory-optimized structure (see Figure 2d), for which we find an inter-layer distance of 18.79 Å. This structure gives rise to diffraction peaks at 0.33 $Å^{-1}$, 2.31 $Å^{-1}$, and 3.96 $Å^{-1}$ in excellent quantitative agreement with the maxima positions found experimentally (namely ~0.33 $Å^{-1}$, ~2.30 $Å^{-1}$, ~3.99 $Å^{-1}$). This is also highlighted in Figure 2b. Apart from the basal spacing related to the lower-angle diffraction maxima, the higher-angle diffraction maxima (labeled in orange and green in Figure 2a) correspond to two distinct spacings of Zn planes within the dense Zn layer indicated in Figure 2e. According to the structural model, the more the thin film was oriented parallel to the substrate surface, the more confined these diffraction maxima would be to the q_r axis. Since this surface orientation is less pronounced in the present case of BPDC-LZH, the intensity maxima are smeared out to rings visible in the multi frame GIWAXS diffractogram. The calculated inter-atomic spacings of 2.72 Å and 1.59 Å agree very well with the experimentally determined values of ~2.73 Å and ~1.57 Å and with experimental observations in the literature.[40,42,73–75] It is noted that the atomistic conformation of our model was inspired by the model of Kurmoo *et al.* for the isostructural layered Cobalt(II) hydroxide with intercalated trans-1,4-cyclohexane dicarboxylic linkers.[77] Notably, the DFT calculations suggested that adsorbed small molecules in the pores of the LZH are important to stabilize the linkers in a vertical orientation, especially with increasing linker length. Otherwise, the linkers would tilt to a nonnegligible degree reducing the inter-layer spacing significantly (see Figure S2 and discussion in Section S1). In fact, in our simulations, four water molecules were included per unit cell to stabilize the orthogonal structure. They are located neighboring dicarboxylates as visible in Figure 2d and Figure S3. The presence of water in the LZH structures has also been experimentally tested by performing a GIWAXS measurement on a thin film sample after dehydration in a vacuum oven. The experimental results are given in Figure S4 and indicate a significant contraction of ZnOH sheets in the LZH phase by ~1 Å which is in very good agreement with observations on the similar structure by Kurmoo *et al.*[77]

To verify that we obtained intercalated LZH by other experiments besides GIWAXS, we also conducted IRRAS experiments on the BPDC-LZH film and show the acquired absorbance spectrum in Figure 3a. Two regions in the spectrum deserve particular attention. These are the broad OH band centered around ~3350 cm^{-1}, and the two carboxylate stretching vibrations around 1400 and 1600 cm^{-1}. Absorption in the band between 3200 to 3570 cm^{-1} is typically attributed to stretching modes of OH groups involved in hydrogen bonds and to stretching modes in free water molecules, whereas the small shoulder at ~3565 cm^{-1} points towards OH stretching without the contributions of H-bonds.[41,78] Both of these features are expected to be present in the LZH structure because of the abundantly present OH groups in the zinc hydroxide sheets and in the water molecules in the pores.[41,42,44,72,74,75,79,80] Additionally, IRRAS performed in ultrahigh vacuum (UHV) allowed us to resolve the OH-band more clearly (Figure S5), and to identify a distinct set of absorption peaks between 3400 and 3600 cm^{-1}. These resemble the data reported by Kurmoo *et al.*,[77] and can be assigned to hydroxyl groups located at different sites of the ZnOH layers, supporting the structure hypothesis. The presence of $BPDC^{2-}$ within the structure is suggested by the observation of symmetric ~1400 cm^{-1} and antisymmetric ~1600 cm^{-1} stretching modes of

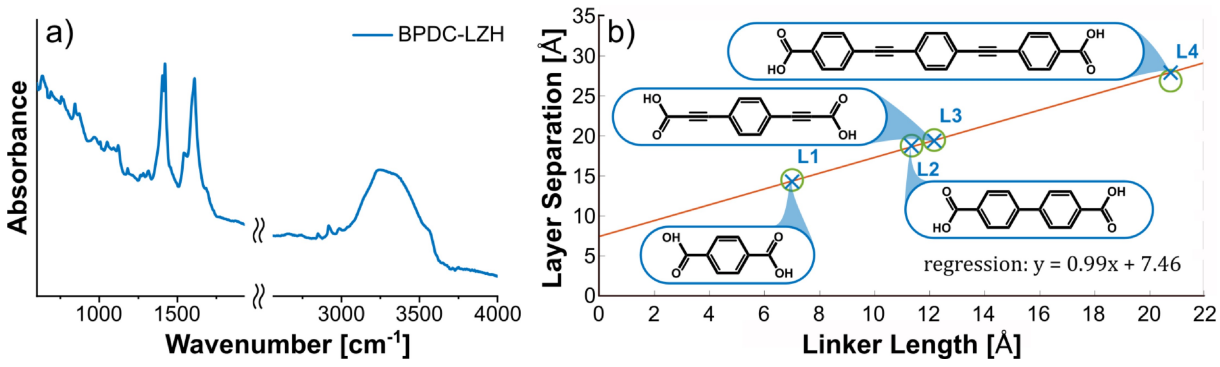

Figure 3. LZH IRRA spectrum and layer separation dependence for different linkers used as pillars separating the zinc hydroxide sheets in the LZH. a) IRRA spectrum of BPDC-LZH showing predominant absorption due to OH groups in a broad band around 3350 cm^{-1} as well as due to symmetric and antisymmetric carboxylate stretching modes around 1400 and 1600 cm^{-1}. A detailed discussion of spectral features is given in the main text. b) Observed layer separation in LZHs *vs.* linker length obtained from molecular simulations with linkers L1–L4 as illustrated in the insets. The experimental data extracted from GIWAXS measurements (blue crosses) very well matches the prediction from the 3D periodic simulations (green circles). Regression of the experimental data points reveals a clear linear dependence with a fitted slope of 0.99 and offset of 7.46 Å, reminiscent of the thickness of ZnOH sheets.

carboxylate, by the small set of peaks around 2900 cm^{-1} characteristic of C–H stretching vibrations,[41,42,72,74,81,82] and by the peak at ~830 cm^{-1} attributed to a 1,4-disubstituted benzene ring vibration.[83] The symmetric and antisymmetric carboxylate stretching absorption bands (~1400 and ~1600 cm^{-1}) containing more than one clear peak could indicate the presence of variable denticity in the coordination between linker and ZnOH sheets.[77,84] Different carboxylate coordination modes could be a direct consequence of the turbostratic disorder discussed earlier.

Now that we have a strong grasp of the thin film fabricated with H_2BPDC at a high excess of Zn^{2+}, we test whether other linkers also form this type of structure when Zn^{2+} ions are abundantly present during synthesis. First, we return to the diffractogram of Zn-BDC in Figure 1c. Testing the experimental basal layer spacing (~14.3 Å) against the value obtained from the DFT-optimized model (14.50 Å) again yields an excellent agreement. This promising result indicates the possibility to tune the basal layer separation of the LZH thin films obtained from layer-by-layer spin-coating by varying the intercalated linker. To test that, in addition to H_2BDC and H_2BPDC (for convenience abbreviated L1 and L2 in the following investigation), we also investigated two longer linkers. These were 3,3′-(1,4-phenylene)bis(2-propynoic acid) (abbreviated L3), a non-polar derivative of the molecules presented by Hamer *et al.*,[85] and 4,4′-(1,4-phenylenebis(ethyne-2,1-diyl))dibenzoic acid (abbreviated L4), as described by Marshall *et al.*[86] The molecular structures of all linkers are shown in the insets of Figure 3b and all samples were fabricated with a Zn^{2+}-to-linker ratio of 50:1. The layer separations were extracted from GIWAXS diffractograms obtained for each thin film (Figure S6), and these experimental values are shown as blue crosses in Figure 3b. We compare these values to the inter-layer distances from DFT-optimized, 3D periodic structural models (containing H_2O guest molecules, *vide supra*), which are plotted as green circles. Again, the experimentally obtained and simulated layer separations agree very well and are directly proportional to the linker length plus an offset. For the latter comparison, the linker length is defined as the O–O distance for isolated linker molecules relaxed in gas phase according to our DFT calculations. Linear regression of the experimental data points reveals a slope of 0.99, which supports the conclusion that the linker orientation is perpendicular to the ZnOH sheet (in all cases, as there are no outliers). The offset of the linear fit of 7.46 Å can be seen as an experimental estimate of the thickness of the zinc hydroxide layers in between the linker molecules. In passing we note, in the case of L4, we could observe a second, minor set of diffraction peaks indicating another, smaller inter-layer spacing (see Figure S6d). We tentatively attribute this to the formation of a second phase with a somewhat contracted structure due to a larger tilt angle of the linker – possibly caused by different amounts of water inside the pores (*cf.* discussion in Section S1).

To generalize and conclude this section, the evidence for all 4 linkers tested forming an LZH when Zn^{2+} is in a high excess in the precursor solution is very strong. The basal spacing of the LZH scales with the length of the linkers, and indicates that the linkers preferentially stand perpendicularly between the zinc hydroxide layers. To our knowledge, this is the first report of using a layer-by-layer spin-coating approach to fabricate LZH thin film structures. It suggests that this facile approach could replace more involved protocols as mentioned in the introduction.

Zn-BDC Metal-Hydroxide-Organic Framework (MHOF)

Having understood that the structures formed in the presence of an excess of the Zn-precursor are not related to SURMOF-2 type structures, raises the question, whether also for Zn-BDC (1:1) a fundamentally different structure is formed. The dissimilarity of the patterns in Figures 1b,c implies that the Zn-BDC (1:1) structure is also not consistent with the formation of an LZH. For determining the actual structure of Zn-BDC (1:1) an equivalent, but better resolved diffraction pattern than that shown in Figure 1b would be highly desirable. Such a pattern can, indeed, be generated for somewhat different fabrication conditions. For displaying consistent data in Figure 1, the results of spin-coating on Si with equimolar precursor ratios at an absolute concentration of 0.1 mM were shown in that figure. A clearer, yet equivalent (see Figure S7), diffraction pattern could be obtained for a Zn-BDC film grown at a concentration of 1 mM on Au surfaces functionalized with carboxylate-terminated 16-mercaptohexadecanoic acid (MHDA) self-assembled monolayers (SAMs). Therefore, we used the latter type of sample to collect the GIWAXS data presented in Figure 4a. In order to identify the structure of the Zn-BDC MOF, we pursued a two step procedure. First, to simplify the comparison between our data and potential structural motifs, we again produced pPXRD patterns by radially integrating the GIWAXS data. Then, we compared the experimental pPXRD data to a variety of simulated PXRD patterns of structures DFT-optimized starting from literature-known compounds and chemically sensible variants thereof. None of these (SUR)MOF-2 derived structures adequately reproduced the experimental data. However, a non-porous Zn-BDC metal-hydroxide-organic framework, derived from a Cu-BDC structure reported by Abdelouhab *et al.* (CCDC-CSD identifier KAKSUL),[87] produced an exceptional agreement (including peaks at higher scattering angles) between our experiments and a powder diffractogram calculated for the simulated structure (Figure 4b). We note that the peak intensities in this comparison are not expected to be equal due to the different geometries in GIWAXS *vs.* PXRD measurements and the fact that properly correcting for the resulting effects is not trivial. The peak positions, however, can be compared and are well matched. In detail, the Zn-BDC structural model was obtained by modifying the original Cu-BDC (KAKSUL) structure file, replacing Cu by Zn and adding hydrogen atoms including one for each of the two unbound oxygen atoms present in the unit cell to ensure charge neutrality. This system then underwent a full, unconstrained geometry optimization relaxing both atomic positions as well as unit cell parameters. The resulting Zn-BDC MHOF structure is shown in Figure 4c. Two different projections are given, with the unit cell in black. The structure is

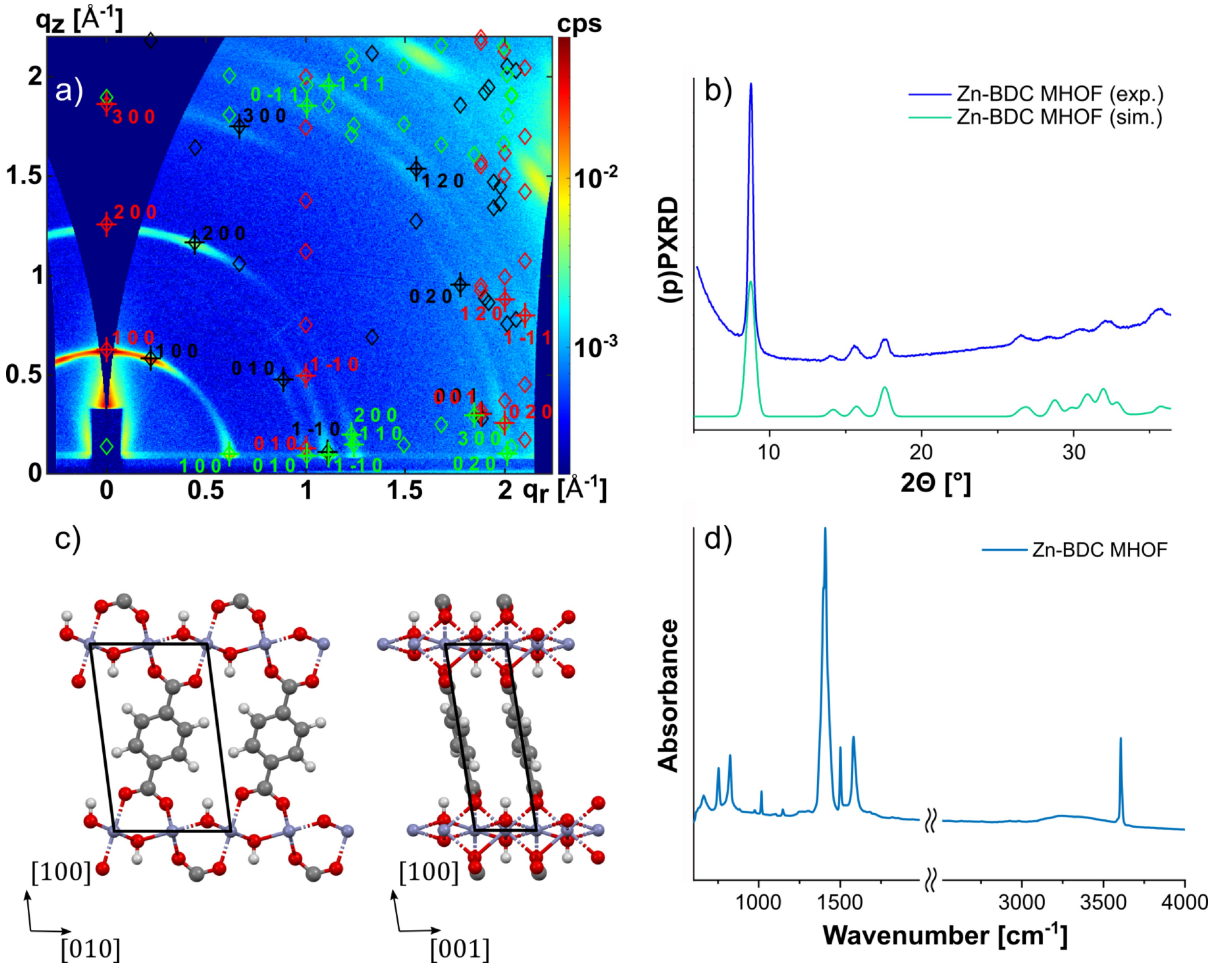

Figure 4. Zn-BDC metal-hydroxide-organic framework (MHOF). a) GIWAXS of Zn-BDC MHOF with Laue indices shown at the positions where correspondence between simulated and experimental pattern is observed. The GIWAXS pattern can be well explained by three dominant thin film orientations on the substrate whose simulated peak positions are indicated in black ((410) orientation), red ((100) orientation) and green ((001) orientation). The lack of experimental scattering peaks with $h > 1$ while $k|l \neq 0$ is an indication of low long-range ordering across multiple sheets. In the top right corner, for $q > \sim 2.5$ Å^{-1}, scattering of the underlying MHDA SAM is visible, which is not related to the thin film. b) Comparison of simulated PXRD pattern and experimental pPXRD pattern, obtained by radial integration of the GIWAXS data. c) Zn-BDC MHOF structural model obtained from *ab initio* calculations consisting of sheets of Zn atoms coordinated with carboxylate groups of bridging BDC^{2-} molecules. d) IRRA spectrum of the same Zn-BDC MHOF thin film. The most prominent peaks around 1500 cm^{-1} and the peak at ~3600 cm^{-1} are indicative of the BDC^{2-} and the OH groups coordinated with the Zn atoms inside the structure.

composed of dense, distorted Zn hydroxide sheets that incorporate the carboxylate groups of the BDC^{2-} linkers on both sides and, thereby, connect neighboring ZnOH sheets.

Since this is the second time we mention ZnOH sheets inside a structure, we emphasize that they are fundamentally different in the MHOF and LZH structures. In the MHOF, Zn and O(H)-groups are situated within a single layer, while in the LZH, there is an entire substructure of the framework consisting of Zn and O(H) groups in octahedral and tetrahedral configuration. Moreover, in the MHOF, all Zn atoms are bonded to oxygens from carboxylates and share OH groups with neighboring Zn atoms. Conversely, in the LZH, most of the Zn atoms are not bonded to linkers at all. This becomes clear comparing Figures 2c and 4c.

Based on the excellent agreement between experimental pPXRD and theoretical PXRD patterns, as a second step, we tested the experimental 2D diffractogram against the diffraction pattern that would arise from the MHOF structure. Multiple maxima on the different diffraction rings point towards more than one preferred texturing of the films. In fact, we were able to identify three dominant growth orientations characterized by the (410), (100) and (001) reciprocal lattice planes parallel to the substrate. The simulated GIWAXS diffraction peak positions resulting from scattering from these three orientations are overlaid in the form of black, red, and green diamond-shaped labels in Figure 4a. The orientation with respect to the substrate for these growth textures is illustrated in Figure S8. In the case of the (001) texture we note that its contribution might easily be overestimated. A significant number of its peaks reside in the region near the horizon where they are intermixed with and, thereby, superelevated by the Yoneda peak.[88] In Figure 4a, all major diffraction peaks in the GIWAXS data can be described by diffraction from one of these textures, with the corresponding Laue indices as indicated in the figure. The agreement

between simulated and experimental diffractograms not only in terms of PXRD but also the GIWAXS pattern clearly supports the assignment that Zn-BDC under the equimolar fabrication conditions forms an MHOF structure. As another qualitative support of the structural hypothesis, we note that our diffraction data on the Zn-BDC MHOF strongly resembles the grazing-incidence XRD data on the isostructural copper hydroxide sheets separated by BDC^{2-} recorded by Stassin *et al.* and made by vapor-phase deposition.[18] Interestingly, we observe in our 2D diffractogram what seems to be a systematic absence of diffraction peaks with an index $|h| > 1$ and $k|l \neq 0$. To picture that more explicitly, we show in Figure S9 the same GIWAXS pattern with these simulated peak positions highlighted. This observation suggests a low long-range order across multiple MHOF sheets. This could hint towards a weak type of turbostratic disorder, like in the case of the LZHs before. Further reasoning behind this idea is added in a later section.

Also for the Zn-BDC MHOF structure, we carried out IRRAS for which the acquired spectrum is presented in Figure 4d. It exhibits a sharp absorption peak at 3606 cm^{-1} located in the range typically assigned to OH stretching modes not involved in hydrogen bonds.[78] This peak corresponds very well to the abundantly present OH groups contained in the Zn hydroxide layers of our structural model. Additionally, we observe a much less pronounced, broad OH-related band around 3240 cm^{-1} which could stem from a small amount of residual ethanol molecules coordinated via hydrogen bonds inside the structure or, possibly, defective sites where (not deprotonated) H_2BDC molecules are attached to OH groups. These observations match the data presented by Yuan *et al.* for their Ni-based structural analog.[71] The peaks at 662, 1017, 1148, 1500 cm^{-1} are attributed to aromatic C–C vibrations and C–H bending modes, while the peak at 753 cm^{-1} corresponds to a phenyl ring deformation.[60,89] These IR absorption peaks in addition to the carboxylate antisymmetric (1581 cm^{-1}) and symmetric stretching modes (1397, 1408 cm^{-1}) are clear evidence for linker incorporation in line with the structural model.

Mixed Growth of Zn-BDC MHOF and LZH

Observing in Figures 1b and 1c that Zn-BDC in neither case resulted in the expected SURMOF-2 type structure, stimulated us to additionally test a broader range of Zn^{2+}-to-BDC^{2-} ratios. Also, to improve surface attachment and, therefore, potentially facilitate the SURMOF-2 type structure formation, we grew the films on carboxylate-terminated MHDA SAMs on Au surfaces. Samples were fabricated with Zn^{2+}-to-linker ratios of 1:10 to 100:1, while always keeping the higher concentrated precursor solution at 1 mM. An overview of all GIWAXS measurements of these samples is provided in Figure S10. Concluding from all the recorded diffractograms, we observe that Zn-BDC never forms the SURMOF-2 type structure when utilizing the stated fabrication protocol. In fact, the result of all syntheses was some combination of the two structures responsible for the diffraction patterns in Figures 1b and 1c, respectively. In fact, we can observe a progression from primary (or even pure) MHOF to primary (or even pure) LZH with an increasing Zn^{2+}-to-BDC^{2-} ratio, including an intermediate region where a film is present with a mix of both structures (10:1 and 50:1 in Figures S9d and S9e). This is in stark contrast to the Cu-based analog, which we also fabricated on MHDA Au for reference over a range of Cu^{2+}-to-BDC^{2-} ratios. For the Cu-case, a structure consistent with the SURMOF-2 literature was always formed (Figure S11), like already seen in Figure 1a. This implies that a SURMOF-2 type structure can be fabricated from Cu and H_2BDC over a wide variety of Cu^{2+}-to-linker ratios, while this is not the case for Zn. There, a pure MHOF is produced at equimolar conditions, a pure LZH film at high Zn excesses, and a mix of the two structures at intermediate concentrations.

Also for the discussed Zn-based sample series, we performed IRRAS measurements and obtained results further supporting the hypothesis that varying fractions of the two distinct structural phases are present in the samples. All IRRA spectra are shown in Figure S12. The absorption spectra of the samples made from mild excess of linker over metal ion bear strong resemblance to the already examined Zn-BDC MHOF spectrum in Figure 4d. Progressing to the spectra of Zn-BDC with increasing excess of Zn^{2+} (10:1 to 100:1), we continue to see the same sharp set of absorption peaks as in the pure MHOF spectrum. However, there is a strong increase of the OH band and shift of its peak towards 3400 cm^{-1}, indicative of significant amount of water stored inside the LZH. Meanwhile, the sharp peak at 3606 cm^{-1} reduces in height, but still remains visible and we see an increasing broadening of the antisymmetric carboxylate stretching peak. To give a telling visual impression of the intermixing of two different IRRA spectra, we show the high resemblance of the 50:1 spectrum with the simple summation of the pure BDC-LZH and Zn-BDC MHOF spectra in Figure S13. All of these observations perfectly match the conclusions we could draw earlier by means of GIWAXS about the fraction of MHOF and LZH structures within the thin films.

In the next section, we will offer an explanation as to why we observe two different types of structures when changing the Zn^{2+} ion-to-linker ratio in the first place.

Hypothesis for Structural Formation Mechanism

In this section, we present some support for a unified hypothesis regarding how the various possible end structures might be formed as the result of a conversion from small Zn hydroxy acetate crystals that are formed on spin-casting of the Zn acetate precursor solution. Spin-casting a single cycle of the Zn acetate precursor does not leave a thick enough film for GIWAXS characterization, but repeated spin-casting of the Zn acetate precursor solution 40 times (without rinsing or spin-casting the linker solution) leads to a crystalline structure that can be characterized by GIWAXS. The GIWAXS diffraction data from this single component, Zn precursor only film is presented in Figure S14a. The diffraction pattern resembles those observed for the LZHs presented earlier, but is extremely oriented along the q_z direction. It also suggests a smaller basal spacing

of ~13.6 Å. Such a basal spacing is a strong evidence for the formation of Zn hydroxy acetate, which is a LZH with acetate anions and water molecules in between the ZnOH sheets.[40–42,72,76,90] Spin-casting Zn acetate dihydrate from ethanol, apparently yields similar structures as using a sol-gel precursor.[61] The structure of such a layer is sketched in the left part of Figure 5. The faster evaporation of ethanol due to its lower boiling point compared to water, could play an important role in the formation of the Zn hydroxy acetate. During spinning, a strong increase in the relative amount of water in the solution on the substrate could be caused by the faster-volatilized ethanol in the ambient atmosphere. Also, the rapid drying caused by the spin-casting seems to play an important role since films that are made by simply drop-casting the Zn precursor solution and drying naturally yield distinctly different structures (see Figure S14b).

From these data, we propose that small crystallites of Zn hydroxy acetate form on the surface of the substrate after each Zn precursor deposition cycle. Upon adding the linker solution, these crystals can either undergo anion exchange leading to a dicarboxylate-intercalated LZH or, with a greater concentration of linkers, be converted to an M(H)OF structure. This hypothesis is illustrated in Figure 5. In the case of Zn-BDC, using the results from varying the molar ratio (in Figures S10 and S12), we can assign approximate reference points to explain this process: A very high metal ion-to-linker ratio (~50:1 or higher) facilitates anion exchange, an equimolar ratio or a mild excess of linker molecules (~1:1 to 1:10) triggers conversion, and a less pronounced excess of Zn (~10:1) allows for both processes to happen in parallel. For the short H_2BDC linker, the energetically favored conversion product is the non-porous metal-hydroxide-organic framework, whereas the longer H_2BPDC linker initiates the formation of a SURMOF-2 type structure. The conversion process happening in each spin-coating cycle could be similar to the synthesis route presented by Kim *et al.*, in which they produce pillared-layer MOF thin films from hydroxy double salt (HDS) intermediates.[91] The obtained MOF system, consisting of Cu, various H_2BDC derivatives and 1,4-diazabicyclo[2.2.2]octane (DABCO), was thereby reported to spontaneously form when exposing a Cu-Zn-HDS precursor layer to a solution containing linker and DABCO pillar molecules, constituting a very similar structural conversion as observed in our work. The authors furthermore argue that linker solubility has an effect on the MOF formation in their synthesis, which could potentially play a role in our thin film fabrication as well.

Based on this suggested transformation process, we can draw conclusions that explain observations discussed earlier in the context of the GIWAXS characterization. We start by recalling that in the 2D diffractograms of BDC-LZH (Figure 1c) and BPDC-LZH (Figure 1f), we noticed the intensity maxima being much more confined to the q_z axis in the case of H_2BDC, thus signifying a much more dominant substrate-parallel arrangement of the LZH sheets than in the case of H_2BPDC. Altering an already flat-lying Zn hydroxy acetate by anion exchange could explain this observation. The small dimensions of the H_2BDC molecule, not much larger than acetic acid, could allow for much easier diffusion into the basal cavities of Zn hydroxy acetate sheets. Thereby, the originally flat orientation

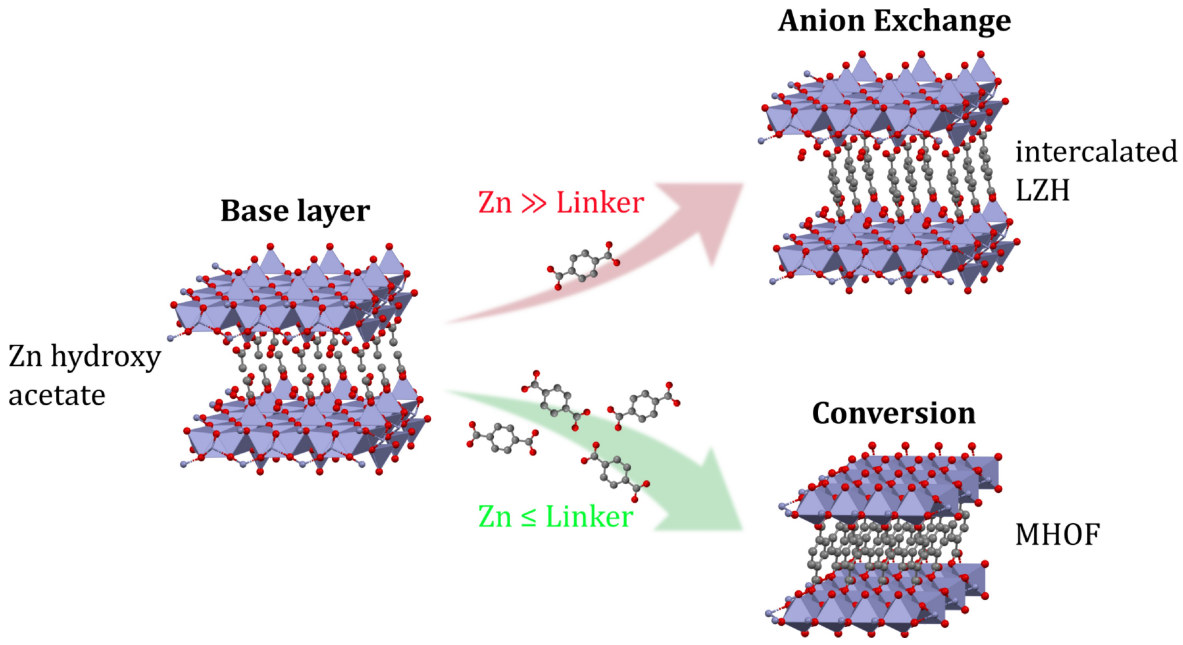

Figure 5. Possible transformation process during layer-by-layer spin-coating from ethanolic Zn acetate dihydrate solution. The figure, exemplarily, illustrates the process for the case of H_2BDC. Deposition of the Zn precursor solution leads to the formation of Zn hydroxy acetate base layers on the substrate upon solvent evaporation during spinning. By the following addition of linker solution, two types of transformations can happen depending on the Zn^{+2}-to-linker ratio. In the case of large excess of Zn^{+2}, linkers will intercalate by anion exchange and replace acetate molecules between Zn hydroxide sheets. An equimolar ratio or mild excess of the linker initiates structural conversion to metal(-hydroxide)-organic frameworks. Depending on the specific linker molecule, different structures can thereby be energetically favored. H_2BPDC leads to SURMOF-2 type structure formation while H_2BDC causes growth of the non-porous MHOF. Mild excess of Zn will allow for both processes to happen simultaneously.

can be largely preserved upon linker intercalation, only increasing the layer separation by ~5%. The significantly longer H_2BPDC molecules, on the other hand, could locally break up the layered structure by expanding smaller defects of the initially flat-lying Zn hydroxy acetate sheets when replacing the acetate groups. This then results in significantly more random orientation observed with GIWAXS. In general we assume that geometric effects associated with the size of the organic linker molecules can influence their infiltration and ordering within the ZnOH sheets during the proposed anion exchange process. Longer linkers like BPDC (11.34 Å), L3 (12.16 Å), or L4 (20.75 Å) are likely less prone to anion exchange and their incorporation in LZH might introduce more defects and a less ordered arrangement of the thin films than in the case of shorter linkers like BDC (7.00 Å). However, even if the anion exchange process in such cases might happen on a longer time scale, we still deem this a plausible mechanism. In this regard, we consider the layer-by-layer growth method an essential factor in mitigating the impact of geometric constraints during the diffusion of the dicarboxylic linkers by requiring intercalation only in a few surface layers at a time per deposition cycle. We now look back at the Zn-BDC growth on MHDA Au, using the new understanding to provide an explanation for the preferred growth of different textures and why certain diffraction peaks ($h>1$ while $k|l\neq 0$) seem to be systematically absent. Starting from the flat-lying Zn hydroxy acetate basis layer for the subsequent conversion to an MHOF, makes a (001)-oriented texture much less likely, since that would require the basis ZnOH layer to tilt by 90 degrees during the conversion process. Consequently, (410) and (100) orientations which do not require massive rotations of the precursor layer, are more dominant. This is obvious for the (100) texture with ZnOH layers parallel to the substrate. The (410) texture, requires a seemingly random small inclination angle of ~20° (indicated in Figure S8a) of the ZnOH layers relative to the substrate plane, which could be related to the carbon chain tilt angle of the underlying MHDA molecules (~24° on average according to literature).[92] The MHOF structure adapting the tilt angle of the SAM molecules strongly supports surface-initiated growth being responsible for the (410) texture. Linking the occurrence of this texture to the presence of the MHDA SAM would also clarify why we cannot observe the characteristic (100), (200) and (300) off-axis diffraction peaks of the MHOF related to the (410) orientation in Figure 1b: there, the diffractogram of Zn-BDC MHOF on Si is shown and the system does not contain any MHDA SAM. Finally, we speculate that the turbostratic disorder of the Zn hydroxy aceate basis layer could be passed on during transformation to the Zn-BDC MHOF, leading to a reduced long-range order of the crystal lattice. This would explain the observed absence of certain diffraction maxima that would require the long-range order across multiple ZnOH layers within the MHOF structure.

Thin Film Photoluminescence

Finally, we demonstrate that PL changes are an easily accessible indicator for the formation of different structures in Zn-based thin films. For example, the PL of the BPDC-LZH thin film is remarkably different than of the SURMOF-2 type structure (*cf.* photo in Figure S15), and shall serve as an exemplary probe for the actually occurring structure in the following discussion. In Figures 6a and 6b, we present the steady-state and time-resolved PL of H_2BPDC in a highly diluted ethanol solution (0.01 mM) compared to its pure powder form and when in the LZH and SURMOF-2 type structures. Furthermore, we measured the photoluminescence quantum yields (PLQYs) of the different structures. They are listed in the inset in Figure 6a. The (slow component) excited state lifetimes extracted from the decay kinetics are summarized in the inset in Figure 6b.

While the emission of H_2BPDC in ethanol peaks at 332 nm, the PL from the thin films is strongly red-shifted, comparable to

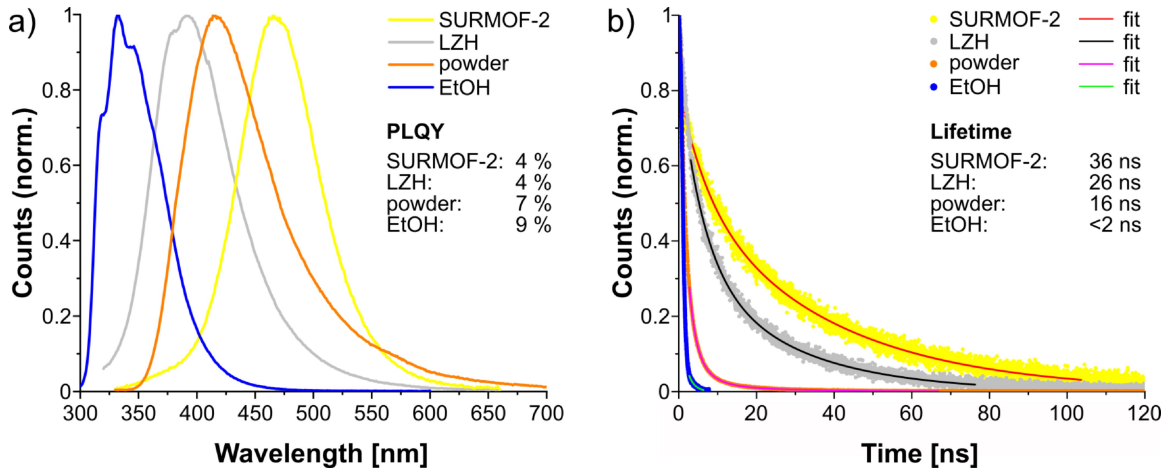

Figure 6. PL of H_2BPDC in different structures. a) Steady-state PL of H_2BPDC in ethanol, in powder form, in LZH, and in SURMOF-2 type structure. For each compound, the photoluminescence quantum yield (PLQY) is given in the small inset. b) Corresponding time-resolved PL acquired by time-correlated single-photon counting (TCSPC) at the respective peak wavelength. The lifetimes of the slowly decaying components of the materials derived from (multi-)exponential fits are indicated as well. Longer-lived aggregate states due to the dense packing of the linker molecules are assumed within LZH and SURMOF-2 type structure, accompanied by a peak emission red-shift that is comparable to H_2BPDC powder.

the emission of pure H_2BPDC powder. The LZH emission is less red-shifted than that of BPDC in its powder form; conversely, the emission from the SURMOF-2 type structure is even more red-shifted than that of the powder. This is consistent with the GIWAXS observations, from which the molecular separation of the chromophores is expected to be significantly larger in the LZH case (likely further enhanced by the turbostratic disorder) than in the SURMOF-2 type structure. In LZH, the maximum emission appears at 391 nm and in the SURMOF-2 type structure even further in the green at 467 nm. This is suggestive of stronger intermolecular interactions in the SURMOF-2 type structure than in the LZH. The peak emission of H_2BPDC powder with 416 nm is located in between the thin film structures. The time-resolved PL measurements reveal that the decay dynamics are no longer mono-exponential in the solid state, supporting the probability that the luminescence comes from intermolecular states. The lifetime is longer for the SURMOF-2 type structure than for the LZH, and both their lifetimes are longer than that of the H_2BPDC powder. We acknowledge the possible red-shifting contribution of re-absorption effects to the observed spectra and decays but conclude in Section S2 that such influences would only be very minor here. Interestingly though, the PLQY of the H_2BPDC powder is higher, indicating that the radiative decay rate of the states in the LZH and SURMOF-2 type structures must be suppressed with respect to that present in the powder. Irrespective of the precise reasons for the differences, the notable differences in PL between the thin film samples (both in terms of spectra and lifetime) are strong indications of a structural change. Similar results were obtained on the Zn-BDC mixed MHOF/LZH sample series and are presented in Figure S16. Corroborating the IRRAS and GIWAXS data discussed earlier, we can see a reflection of the mixed-phase thin film nature in the emission spectra appearing as a superposition of pure MHOF and LZH emission spectra. Uniform emission captured with a microscope objective at different positions across such a mixed-phase Zn-BDC sample, thereby, points towards a macroscopically homogeneous distribution of the MHOF and LZH grains across the coated substrate area. Beyond corroborating the GIWAXS analysis, a sudden change in PL behavior between different thin films serves as an easy-to-observe warning sign that structural changes may also occur.

Conclusions

In this work, we have combined GIWAXS and DFT calculations to demonstrate that the frequently used layer-by-layer spin-coating technique based on Zn acetate dihydrate as a metal precursor often does not lead to the formation of SURMOF-2 type structures. For Zn-BPDC, the formation of such a structure occurs given an equimolar ratio of precursors. Conversely, for the shorter linker in Zn-BDC, we could never observe the formation of a SURMOF-2 type structure *via* spin-coating. Instead, we found strong evidence for the formation of an MHOF for a Zn^{2+}-to-linker ratio ≤ 1. In this structure, Zn^{2+} ions within a single ZnOH layer are directly connected to BDC^{2-} from two sides. For a high excess of Zn^{2+}, we find that crystalline intercalated LZH films are formed exclusively. These structures exhibit extended ZnOH layers, comprising distinct octahedral and tetrahedral atomic arrangements. These layers are separated by organic spacer molecules. The intercalated LZHs can be synthesized with a variety of dicarboxylic acids, including molecules that are much longer than BDC^{2-} and $BPDC^{2-}$ such that the choice of the organic spacer can be used to tune the distance between the ZnOH planes. At intermediate Zn^{2+}-to-linker ratios, mixed films were observed containing both LZH and MHOF structures. The determination of the newly identified structures was accomplished by excellent convergence of experimental GIWAXS results and simulation results from DFT calculations. Regarding the photoluminescence of BPDC-LZH and SURMOF-2 type structures, differences in spectra and lifetimes are apparent. In Zn-BDC thin films, the compound nature of intermixed MHOF/LZH structures is reflected also in their emission characteristics. Thus, PL differences amongst crystalline films of the same linker under different synthesis conditions can raise a warning flag that different structures are being obtained. In terms of mechanistic understanding, we hypothesize that spin-coating the Zn acetate dihydrate precursor leads to layered zinc hydroxide with intercalated acetate molecules. Then, in the subsequent casting of the linker solution either 1) an anion exchange of the acetic acid with the linker takes place if the Zn is in excess, or 2) a conversion to a MOF or MHOF occurs, when there is sufficient amount of linker molecules available. These findings emphasize the need for careful structural investigations of metal-organic thin films in general, and for Zn-based SBUs in particular. Especially the combination of structural modeling and careful experimental sample characterization have proven extremely useful to find and verify structural hypotheses for such crystalline thin films.

Experimental Section

Thin Film Synthesis by Spin-Coating

Zn acetate dihydrate and Cu acetate monohydrate (EMSURE ACS reagents), benzene-1,4-dicarboxylic acid (H_2BDC) (98%) and biphenyl-4,4′-dicarboxylic acid (H_2BPDC) (98%) were purchased from Merck, Sigma-Aldrich and Acros Organics. 3,3′-(1,4-phenylene)bis(2-propynoic acid) and 4,4′-(1,4-phenylenebis(ethyne-2,1-diyl))dibenzoic acid according to references[85,86] were supplied by the respective authors. The metal precursors and dicarboxylic linkers were dissolved in absolute ethanol upon ultra-sonication and heating up to 55 °C in the desired concentrations. Silicon substrates were rinsed with ethanol, dried by a nitrogen stream and exposed to a UV ozone plasma for at least 15 mins. Substrates with functional SAM were prepared by immersion of ethanol-rinsed 100 nm Au on Si substrates in a 0.02 mM MHDA ethanolic solution for 2 days, rinsed with ethanol and also dried with nitrogen. The spin-coating protocol comprised alternating casting of metal precursor solution and linker solution and intermediate rinsing with pure ethanol in ambient conditions. The spin-coating parameters were 10 s total spinning time per drop-cast with an acceleration of 500 rpm/s and a maximum speed of 2000 rpm. The approximate substrate size was 1 cm by 1 cm. A typical synthesis comprises 40 cycles of alternating casting of metal solution, pure ethanol, linker

solution and pure ethanol. Although we note that even with much fewer cycles we can still see clear structures during GIWAXS characterization.

Grazing-Incidence Wide-Angle X-Ray Scattering (GIWAXS)

The structural characterization of the thin film samples via GIWAXS was performed under ambient conditions on a Bruker D8 Advance (primary track: unpolarized Cu K-alpha X-ray source at 40 kV and 40 mA, Goebel mirror, 0.5 mm micro mask, 0.3 mm snout; secondary track: DECTRIS Eiger2 R 500 2D detector; sample-detector distance 118.1 mm). The incidence angle and exposure time of every presented GIWAXS measurement is given in Table S1. Data analysis was performed similar to the procedure shown previously, where we stitch diffraction patterns acquired at distinct detector positions together and project them onto a common vertical detector plane.[31] Polarization correction (unpolarized source), 2D image reshaping to reciprocal q_z-q_r-space and calculation of peak positions according to structural simulation was carried out using the GIXSGUI MATLAB toolboox.[70] More details on the simulated diffraction patterns are supplied in Section S3.

Photoluminescence Spectroscopy

The emission characteristics of Zn-BPDC thin film samples, H_2BPDC in ethanol and H_2BDC powder were measured with an Edinburgh Instruments FS5 Fluoresence Spectrometer using the pre-installed broad-band Xenon lamp. For time-dependent TCSPC PL measurements an external picosecond pulsed light-emitting diode (EPLED) operating at 260 nm with a pulse width of 900 ps and variable repetition rate was used. The emission decays acquired by TCSPC were fitted using the Edinburgh Instruments Fluoracle software. More details on the fitting are supplied in Section S4. The Zn-BDC thin film PL was recorded by a fiber-coupled (Thorlabs BFY400MS02) Avantes AvaSpec-ULS2048x64TEC-EVO spectrometer upon excitation with a Thorlabs M300 L4 light-emitting diode (LED). The local PL probing was performed by using an infinity-corrected Nikon TU Plan ELWD (Magnification 100×, Numerical Aperture 0.8) along with a fiber-coupled (Thorlabs FP1000URT, high OH) Ocean Insight QEPro spectrometer and the same excitation source.

UV-Vis Absorption Spectroscopy

The absorbance spectrum of H_2BPDC in ethanol was acquired with an Agilent Cary 7000 Universal Measurement Spectrophotometer (UMS) with the sample solution situated in a quartz cuvette. The spectra of the Zn-BPDC thin films were measured in diffuse reflectance mode with the samples mounted inside an integrating sphere.

Infrared (IR) Spectroscopy

The IRRA spectra were obtained using a Bruker VERTEX 80v Fourier-transform IR (FTIR) spectrometer with a liquid nitrogen-cooled mercury cadmium telluride narrow band detector at a resolution of 2 cm^{-1}. The measurements were performed in grazing incidence reflection mode using an incidence angle of 10° with respect to the substrate plane. Background subtraction was carried out based on reference measurements of perdeuterated hexadecanethiol SAMs on Au. UHV-FTIR measurements were performed with an apparatus that combines a multichamber UHV system (Prevac) and an FTIR spectrometer (Bruker Vertex 80v). The samples were first pressed into an inert metal mesh and mounted on a sample holder optimized for UHV IR measurements. The base pressure in the sample chamber was ~1 e^{-10} mbar.

Photoluminescence Quantum Yield

The samples were situated in an integrating sphere (15 cm diameter) excited with a Thorlabs M300 L4 light-emitting diode (LED) at 300 nm wavelength with appropriate band pass filter. The emitted light was focussed into an optical fiber (Thorlabs BFY400MS02) and analyzed by an Avantes AvaSpec-2048×64TEC spectrometer.

Structure Computation

All DFT calculations were executed with FHI-aims version 221103–1.[93–96] The Perdew-Burke-Ernzerhof functional,[97] in combination with the nonlocal many-body dispersion correction,[98] was used. Default'tight' basis sets as implemented in the FHI-aims code were applied for all atomic species. For the occupation of Kohn-Sham eigenstates, a Gaussian broadening with a width of 10 meV was used.[99] The net total charge was constrained to 0, and no spin was considered explicitly. Relativistic effects were accounted for using the atomic ZORA approximation.[100] In all geometry optimizations, both atomic coordinates as well as unit cell parameters were optimized without constraints, using the trust radius enhanced BFGS optimization algorithm.[101] For the MHOF calculations, a k-grid of 2×2×7 points was employed. Self-consistency convergence settings for the forces, charge density, and total energy were set to 10^{-4} eV/Å, 10^{-5} a_0^{-3}, and 10^{-6} eV, respectively. For the structural relaxation, a force tolerance of 10^{-2} eV/Å was used. For all LZH, except for L4-LZH with H_2O, a k-grid of 2×1×3 was employed. In case of L4-LZH with H_2O, the k-grid density was doubled to circumvent SCF nonconvergence. Self-consistency convergence settings for the charge density and total energy were set to 10^{-6} a_0^{-3}, and 10^{-7} eV, respectively. For the structural relaxation, a force tolerance of 5×10^{-3} eV/Å was used. All DFT calculations were executed on the Vienna Scientific Cluster (VSC) 5. Computation files are available *via* the TU Graz repository (https://doi.org/10.3217/3378f–2e492).

Deposition Numbers 2349062-2349070 contain the supplementary crystallographic data for this paper. These data are provided free of charge by the joint Cambridge Crystallographic Data Centre and Fachinformationszentrum Karlsruhe Access Structures service.

Supporting Information

Supporting Information is available from the Wiley Online Library or from the author.

Acknowledgements

We gratefully acknowledge the DFG for funding through the priority program SPP 1928 COORNETS, as well as the Helmholtz Association for funding through i) HEMF, ii) the MTET program (Materials and Technologies for the Energy Transition) – Topic 1 – Photovoltaics (38.01.05), and iii) the recruitment initiative of B.S.R. Furthermore, we thank the Karlsruhe School of Optics and Photonics (KSOP) and the Ministry of Science, Research and the Arts of Baden-Württemberg (Excellence Initiative II) and the

TU Graz Lead Project 'Porous Materials @ Work for Sustainability' (PMWS-LP03) for supporting this work. We thank Rainer Herges and Ross Forgan for supplying the linker molecules, Dmitry Busko for help with the PLQY measurements, Eric Sauter for his technical support during UHV-FTIR measurements, Nina Vankova and Narges Taghizadeh for stimulating discussions regarding possible SURMOF-2 type configurations of Zn-BDC, and Roland Resel and Mario Fratschko for advice in GIWAXS simulation and interpretation. The presented computational results have been achieved using the Vienna Scientific Cluster (VSC). Open Access funding enabled and organized by Projekt DEAL.

Conflict of Interests

The authors declare no conflict of interest.

Data Availability Statement

The data that support the findings of this study are available from the corresponding author upon reasonable request.

Keywords: metal-organic framework · layer-by-layer · GIWAXS · DFT · ab initio

[1] W. P. Lustig, S. Mukherjee, N. D. Rudd, A. V. Desai, J. Li, S. K. Ghosh, *Chem. Soc. Rev.* **2017**, *46*, 3242.
[2] Q. Zhang, C. F. Wang, Y. K. Lv, *Analyst* **2018**, *143*, 4221.
[3] T. N. Nguyen, F. M. Ebrahim, K. C. Stylianou, *Coord. Chem. Rev.* **2018**, *377*, 259.
[4] R. Li, S. H. Wang, Z. F. Liu, X. X. Chen, Y. Xiao, F. K. Zheng, G. C. Guo, *Crystal Growth and Design* **2016**, *16*, 3969.
[5] Y. Zheng, F. Z. Sun, X. Han, J. Xu, X. H. Bu, *Adv. Opt. Mater.* **2020**, *8*, 1.
[6] X. Hu, Z. Wang, B. Lin, C. Zhang, L. Cao, T. Wang, J. Zhang, C. Wang, W. Lin, *Chem. Eur. J.* **2017**, *23*, 8390.
[7] Y. Zorlu, L. Wagner, P. Tholen, M. M. Ayhan, C. Bayraktar, G. Hanna, A. O. Yazaydin, Ö. Yavuzçetin, G. Yücesan, *Adv. Opt. Mater.* **2022**, *10*, 1.
[8] C. Liang, L. Cheng, S. Zhang, S. Yang, W. Liu, J. Xie, M. D. Li, Z. Chai, Y. Wang, S. Wang, *J. Am. Chem. Soc.* **2022**, *144*, 2189.
[9] J. Liu, Y. Chen, X. Feng, R. Dong, *Small Structures* **2022**, *3*, 2100210.
[10] R. Zheng, Z.-H. Fu, W.-H. Deng, Y. Wen, A.-Q. Wu, X.-L. Ye, G. Xu, *Angew. Chem. Int. Ed.* **2022**, *61*, e202212797.
[11] H. Arora, R. Dong, T. Venanzi, J. Zscharschuch, H. Schneider, M. Helm, X. Feng, E. Cánovas, A. Erbe, *Adv. Mater.* **2020**, *32*.
[12] S. Liu, Y. C. Wang, C. M. Chang, T. Yasuda, N. Fukui, H. Maeda, P. Long, K. Nakazato, W. B. Jian, W. Xie, K. Tsukagoshi, H. Nishihara, *Nanoscale* **2020**, *12*, 6983.
[13] C. C. Chueh, C. I. Chen, Y. A. Su, H. Konnerth, Y. J. Gu, C. W. Kung, K. C. Wu, *J. Mater. Chem. A* **2019**, *7*, 17079.
[14] M. A. Gordillo, D. K. Panda, S. Saha, *ACS Appl. Mater. Interfaces* **2019**, *11*, 3196.
[15] J. Liu, C. Wöll, *Chem. Soc. Rev.* **2017**, *46*, 5730.
[16] P. Falcaro, K. Okada, T. Hara, K. Ikigaki, Y. Tokudome, A. W. Thornton, A. J. Hill, T. Williams, C. Doonan, M. Takahashi, *Nat. Mater.* **2017**, *16*, 342.
[17] E. Virmani, J. M. Rotter, A. Mähringer, T. Von Zons, A. Godt, T. Bein, S. Wuttke, D. D. Medina, *J. Am. Chem. Soc.* **2018**, *140*, 4812.
[18] T. Stassin, S. Rodríguez-Hermida, B. Schrode, A. J. Cruz, F. Carraro, D. Kravchenko, V. Creemers, I. Stassen, T. Hauffman, D. De Vos, P. Falcaro, R. Resel, R. Ameloot, *Chem. Commun.* **2019**, *55*, 10056.
[19] D.-H. Chen, H. Gliemann, C. Wöll, *Chemical Physics Reviews* **2023**, *4*.
[20] J. L. Zhuang, M. Kind, C. M. Grytz, F. Farr, M. Diefenbach, S. Tussupbayev, M. C. Holthausen, A. Terfort, *J. Am. Chem. Soc.* **2015**, *137*, 8237.
[21] B. D. McCarthy, T. Liseev, A. M. Beiler, K. L. Materna, S. Ott, *ACS Appl. Mater. Interfaces* **2019**, *11*, 38294.
[22] Z. G. Gu, A. Pfriem, S. Hamsch, H. Breitwieser, J. Wohlgemuth, L. Heinke, H. Gliemann, C. Wöll, *Microporous Mesoporous Mater.* **2015**, *211*, 82.
[23] J. Liu, B. Lukose, O. Shekhah, H. K. Arslan, P. Weidler, H. Gliemann, S. Bräse, S. Grosjean, A. Godt, X. Feng, K. Müllen, I. B. Magdau, T. Heine, C. Wöll, *Sci. Rep.* **2012**, *2*, 1.
[24] M. Oldenburg, A. Turshatov, D. Busko, S. Wollgarten, M. Adams, N. Baroni, A. Welle, E. Redel, C. Wöll, B. S. Richards, I. A. Howard, *Adv. Mater.* **2016**, *28*, 8477.
[25] R. Haldar, M. Kozlowska, M. Ganschow, S. Ghosh, M. Jakoby, H. Chen, F. Ghalami, W. Xie, S. Heidrich, Y. Tsutsui, J. Freudenberg, S. Seki, I. A. Howard, B. S. Richards, U. H. Bunz, M. Elstner, W. Wenzel, C. Wöll, *Chem. Sci.* **2021**, *12*, 4477.
[26] K. Otsubo, T. Haraguchi, O. Sakata, A. Fujiwara, H. Kitagawa, *J. Am. Chem. Soc.* **2012**, *134*, 9605.
[27] T. Haraguchi, K. Otsubo, O. Sakata, A. Fujiwara, H. Kitagawa, *J. Am. Chem. Soc.* **2016**, *138*, 16787.
[28] S. Wannapaiboon, A. Schneemann, I. Hante, M. Tu, K. Epp, A. L. Semrau, C. Sternemann, M. Paulus, S. J. Baxter, G. Kieslich, R. A. Fischer, *Nat. Commun.* **2019**, *10*.
[29] P. Thissen, J. Wohlgemuth, P. Weidler, D. Smilgies, L. Heinke, N. Schewe, M. Koenig, P. Krolla, C. Wöll, *Adv. Funct. Mater.* **2023**, *2301535*, 1.
[30] P. I. Scheurle, A. Mähringer, A. Biewald, A. Hartschuh, T. Bein, D. D. Medina, *Chem. Mater.* **2021**, *33*, 5896.
[31] J. C. Fischer, C. Li, S. Hamer, L. Heinke, R. Herges, B. S. Richards, I. A. Howard, *Adv. Mater. Interfaces* **2023**, *10*, 2202259.
[32] R. Haldar, M. Jakoby, A. Mazel, Q. Zhang, A. Welle, T. Mohamed, P. Krolla, W. Wenzel, S. Diring, F. Odobel, B. S. Richards, I. A. Howard, C. Wöll, *Nat. Commun.* **2018**, *9*, 1.
[33] M. Adams, N. Baroni, M. Oldenburg, F. Kraffert, J. Behrends, R. W. Macqueen, R. Haldar, D. Busko, A. Turshatov, G. Emandi, M. O. Senge, C. Wöll, K. Lips, B. S. Richards, I. A. Howard, *Phys. Chem. Chem. Phys.* **2018**, *20*, 29142.
[34] S. Friedländer, J. Liu, M. Addicoat, P. Petkov, N. Vankova, R. Rüger, A. Kuc, W. Guo, W. Zhou, B. Lukose, Z. Wang, P. G. Weidler, A. Pöppl, M. Ziese, T. Heine, C. Wöll, *Angew. Chem. Int. Ed.* **2016**, *55*, 12683.
[35] A. Nefedov, C. Li, K. Müller, A. B. Kanj, L. Heinke, C. Luo, K. Chen, F. Radu, E. Golias, W. Kuch, C. Wöll, *Phys. Rev. B* **2023**, *107*, 54433.
[36] H. I. Song, J. Bae, E. J. Lee, K. O. Kirlikovali, O. K. Farha, N. C. Jeong, *J. Phys. Chem. C* **2020**, *124*, 13187.
[37] V. Stavila, A. A. Talin, M. D. Allendorf, *Chem. Soc. Rev.* **2014**, *43*, 5994.
[38] G. G. C. Arizaga, K. G. Satyanarayana, F. Wypych, *Solid State Ionics* **2007**, *178*, 1143.
[39] S. Nakagaki, G. S. Machado, J. F. Stival, E. Henrique dos Santos, G. M. Silva, F. Wypych, *Prog. Solid State Chem.* **2021**, *64*.
[40] E. Hosono, S. Fujihara, T. Kimura, H. Imai, *J. Colloid Interface Sci.* **2004**, *272*, 391.
[41] T. Biswick, W. Jones, A. Pacuła, E. Serwicka, J. Podobinski, *Solid State Sci.* **2009**, *11*, 330.
[42] L. Schlur, A. Carton, G. Pourroy, *Chem. Commun.* **2015**, *51*, 3367.
[43] H. Morioka, H. Tagaya, M. Karasu, J. I. Kadokawa, K. Chiba, *J. Mater. Res.* **1998**, *13*, 848.
[44] S. P. Newman, W. Jones, *J. Solid State Chem.* **1999**, *148*, 26.
[45] M. Ramli, M. Z. Hussein, K. Yusoff, *Int. J. Nanomed.* **2013**, *8*, 297.
[46] A. F. Abdul Latip, M. Z. Hussein, J. Stanslas, C. C. Wong, R. Adnan, *Chemistry Central Journal* **2013**, *7*, 1.
[47] J. Liu, X. Zhang, Y. Zhang, *ACS Appl. Mater. Interfaces* **2015**, *7*, 11180.
[48] J. Demel, P. Kubát, I. Jirka, P. Kovář, M. Pospíšil, K. Lang, *J. Phys. Chem. C* **2010**, *114*, 16321.
[49] A. C. T. Cursino, J. E. F. d C Gardolinski, F. Wypych, *J. Colloid Interface Sci.* **2010**, *347*, 49.
[50] A. C. T. Cursino, V. Rives, G. G. C. Arizaga, R. Trujillano, F. Wypych, *Mater. Res. Bull.* **2015**, *70*, 336.
[51] S. Peulon, D. Lincot, *J. Electrochem. Soc.* **1998**, *145*, 864.
[52] D. Pradhan, K. T. Leung, *Langmuir* **2008**, *24*, 9707.
[53] F. Xu, M. Dai, Y. Lu, L. Sun, *J. Phys. Chem. C* **2010**, *114*, 2776.
[54] J. Qiu, M. Guo, X. Wang, *ACS Appl. Mater. Interfaces* **2011**, *3*, 2358.
[55] H. Chen, L. Zhu, H. Liu, W. Li, *Thin Solid Films* **2013**, *534*, 205.

[56] S. Emin, M. Fanetti, F. F. Abdi, D. Lisjak, M. Valant, R. Van De Krol, B. Dam, *ACS Appl. Mater. Interfaces* **2013**, *5*, 1113.
[57] T. Shinagawa, M. Watanabe, J. I. Tani, M. Chigane, *Cryst. Growth Des.* **2017**, *17*, 3826.
[58] H. Chen, L. Zhu, H. Liu, W. Li, *Electrochim. Acta* **2013**, *105*, 289.
[59] H. Nishizawa, K. Yuasa, *J. Solid State Chem.* **1998**, *141*, 229.
[60] S. Inoue, S. Fujihara, *Inorg. Chem.* **2011**, *50*, 3605.
[61] J. B. Miller, H. J. Hsieh, B. H. Howard, E. Broitman, *Thin Solid Films* **2010**, *518*, 6792.
[62] Q. Li, J. Gies, X. J. Yu, Y. Gu, A. Terfort, M. Kind, *Chem. Eur. J.* **2020**, *26*, 5185.
[63] O. Shekhah, *Materials* **2010**, *3*, 1302.
[64] H. K. Arslan, O. Shekhah, D. C. Wieland, M. Paulus, C. Sternemann, M. A. Schroer, S. Tiemeyer, M. Tolan, R. A. Fischer, C. Wöll, *J. Am. Chem. Soc.* **2011**, *133*, 8158.
[65] D. Zacher, K. Yusenko, A. Bétard, S. Henke, M. Molon, T. Ladnorg, O. Shekhah, B. Schüpbach, T. Dea Losa Arcos, M. Krasnopolski, M. Meilikhov, J. Winter, A. Terfort, C. Wöll, R. A. Fischer, *Chem. Eur. J.* **2011**, *17*, 1448.
[66] A. Nefedov, R. Haldar, Z. Xu, H. Kühner, D. Hofmann, D. Goll, B. Sapotta, S. Hecht, M. Krstić, C. Rockstuhl, W. Wenzel, S. Bräse, P. Tegeder, E. Zojer, C. Wöll, *Adv. Mater.* **2021**, *33*, 1.
[67] S. Goswami, M. Rimoldi, R. Anderson, C. Lee, X. Li, A. Li, P. Deria, L. X. Chen, R. D. Schaller, D. A. Gómez-Gualdrón, O. K. Farha, J. T. Hupp, *Chem. Mater.* **2022**, *34*, 9446–9454.
[68] V. Chernikova, O. Shekhah, M. Eddaoudi, *ACS Appl. Mater. Interfaces* **2016**, *8*, 20459.
[69] X. Liu, M. Kozlowska, T. Okkali, D. Wagner, T. Higashino, G. Brenner-Weiß, S. M. Marschner, Z. Fu, Q. Zhang, H. Imahori, S. Bräse, W. Wenzel, C. Wöll, L. Heinke, *Angew. Chem. Int. Ed.* **2019**, *58*, 9590.
[70] Z. Jiang, *J. Appl. Crystallogr.* **2015**, *48*, 917.
[71] S. Yuan, J. Peng, B. Cai, Z. Huang, A. T. Garcia-Esparza, D. Sokaras, Y. Zhang, L. Giordano, K. Akkiraju, Y. G. Zhu, R. Hübner, X. Zou, Y. Román-Leshkov, Y. Shao-Horn, *Nat. Mater.* **2022**, *21*, 673.
[72] A. Moezzi, M. B. Cortie, R. Shimmon, A. M. McDonagh, *Eur. J. Inorg. Chem.* **2013**, *2013*, 5133.
[73] A. H. Leung, S. D. Pike, A. J. Clancy, H. C. Yau, W. J. Lee, K. L. Orchard, M. S. Shaffer, C. K. Williams, *Chem. Sci.* **2018**, *9*, 2135.
[74] S. A. Said, C. S. Roberts, J. K. Lee, M. S. Shaffer, C. K. Williams, *Adv. Funct. Mater.* **2021**, *31*, 2102631.
[75] L. Poul, N. Jouini, F. Fievet, *Chem. Mater.* **2000**, *12*, 3123.
[76] J. T. Rajamathi, N. H. Raviraj, M. F. Ahmed, M. Rajamathi, *Solid State Sci.* **2009**, *11*, 2080.
[77] M. Kurmoo, H. Kumagai, S. M. Hughes, C. J. Kepert, *Inorg. Chem.* **2003**, *42*, 6709.
[78] H. D. Lutz, *Hydroxide ions in condensed materials – Correlation of spectroscopic and structural data*, pages 85–103, Springer Berlin Heidelberg, Berlin, Heidelberg **1995**.
[79] M. Z. bin Hussein, M. Y. Ghotbi, A. H. Yahaya, M. Z. Abd Rahman, *Mater. Chem. Phys.* **2009**, *113*, 491.
[80] A. Gordeeva, Y.-J. Hsu, I. Z. Jenei, P. H. Brant Carvalho, S. I. Simak, O. Andersson, U. Häussermann, *ACS Omega* **2020**, *5*, 17617.
[81] I. Fleming, D. Williams, *Spectroscopic Methods in Organic Chemistry*, vol. 7, Springer Cham **2019**.
[82] K. Saito, T. Xu, H. Ishikita, *J. Phys. Chem. B* **2022**, *126*, 4999.
[83] M. Hesse, H. Meier, B. Zeeh, *Spectroscopic Methods in Organic Chemistry*, vol. 2, Georg Thieme Verlag KG **2008**.
[84] H. Kumagai, M. Akita-Tanaka, K. Inoue, M. Kurmoo, *J. Mater. Chem.* **2001**, *11*, 2147.
[85] S. Hamer, F. Röhricht, M. Jakoby, I. A. Howard, X. Zhang, C. Näther, R. Herges, *Beilstein J. Org. Chem.* **2019**, *15*, 1331.
[86] R. J. Marshall, Y. Kalinovskyy, S. L. Griffin, C. Wilson, B. A. Blight, R. S. Forgan, *J. Am. Chem. Soc.* **2017**, *139*, 6253.
[87] S. Abdelouhab, M. François, E. Elkaim, P. Rabu, *Solid State Sci.* **2005**, *7*, 227.
[88] Y. Yoneda, *Phys. Rev.* **1963**, *131*, 2010.
[89] K. Tan, N. Nijem, P. Canepa, Q. Gong, J. Li, T. Thonhauser, Y. J. Chabal, *Chem. Mater.* **2012**, *24*, 3153.
[90] A. Kawai, Y. Sugahara, I. Y. Park, K. Kuroda, C. Kato, *Ceram. Trans.* **1991**, *22*, 75.
[91] K. J. Kim, J. E. Ellis, B. H. Howard, P. R. Ohodnicki, *ACS Appl. Mater. Interfaces* **2021**, *13*, 2062.
[92] R. Arnold, W. Azzam, A. Terfort, C. Wöll, *Langmuir* **2002**, *18*, 3980.
[93] V. Blum, R. Gehrke, F. Hanke, P. Havu, V. Havu, X. Ren, K. Reuter, M. Scheffler, *Comput. Phys. Commun.* **2009**, *180*, 2175.
[94] F. Knuth, C. Carbogno, V. Atalla, V. Blum, M. Scheffler, *Comput. Phys. Commun.* **2015**, *190*, 33.
[95] V. W.-z. Yu, F. Corsetti, A. García, W. P. Huhn, M. Jacquelin, W. Jia, B. Lange, L. Lin, J. Lu, W. Mi, et al., *Comput. Phys. Commun.* **2018**, *222*, 267.
[96] V. Havu, V. Blum, P. Havu, M. Scheffler, *J. Comput. Phys.* **2009**, *228*, 8367.
[97] J. P. Perdew, K. Burke, M. Ernzerhof, *Phys. Rev. Lett.* **1996**, *77*, 3865.
[98] J. Hermann, A. Tkatchenko, *Phys. Rev. Lett.* **2020**, *124*, 146401.
[99] C.-L. Fu, K.-M. Ho, *Phys. Rev. B* **1983**, *28*, 5480.
[100] E. v Lenthe, E.-J. Baerends, J. G. Snijders, *J. Chem. Phys.* **1993**, *99*, 4597.
[101] J. Nocedal, S. J. Wright, *Numerical Optimization*, vol. 2, Springer New York, NY **2006**.

Manuscript received: March 8, 2024
Accepted manuscript online: April 20, 2024
Version of record online: ■■, ■■

RESEARCH ARTICLE

The structures of metal-organic thin films obtained from layer-by-layer spin-coating are determined by combining grazing-incidence wide-angle X-ray scattering and *ab initio* density functional theory simulations. The Zn^{2+}-to-dicarboxylic linker molar ratio used for spin-coating pivotally influences the resulting structure. High excess of Zn^{2+} generates dicarboxylate-intercalated layered zinc hydroxides, whereas equimolar ratios or slight excess of the linker yield metal-(hydroxide-)organic frameworks.

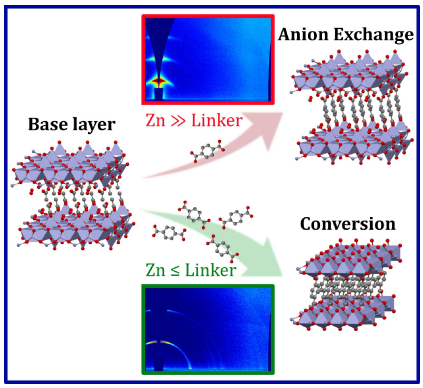

J. C. Fischer, R. Steentjes, Dr. D.-H. Chen, Prof. Dr. B. S. Richards, Prof. Dr. E. Zojer*, Prof. Dr. C. Wöll, Dr. I. A. Howard**

1 – 16

Determining Structures of Layer-by-Layer Spin-Coated Zinc Dicarboxylate-Based Metal-Organic Thin Films